Catalysis Science & Technology

ROYAL SOCIETY OF CHEMISTRY

PAPER

View Article Online
View Journal | View Issue

Published on 26 January 2018. Downloaded by University Town Library of Shenzhen on 3/16/2026 1:55:49 AM.

Check for updates

Cite this: *Catal. Sci. Technol.*, 2018, **8**, 1357

# Conductive Nb-doped $TiO_2$ thin films with whole visible absorption to degrade pollutants†

Xiaoyang Yang, Yuxin Min, Sibai Li, Dawei Wang, Zongwei Mei,*
Jun Liang and Feng Pan *

Received 25th December 2017,
Accepted 25th January 2018

DOI: 10.1039/c7cy02614e

rsc.li/catalysis

Titanium dioxide ($TiO_2$) is widely applied as a photocatalyst; however, its widespread use is limited by its wide band gap; moreover, it is challenging and interesting to make $TiO_2$ absorb the whole range of visible light. In this study, conductive Nb-doped $TiO_2$ (NTO) thin films have been demonstrated to increase the photocatalytic performance of anatase $TiO_2$ due to whole visible-light absorption and efficient charge transfer. Interestingly, the origin of the whole visible absorption was ascribed to the extended free-carrier absorption (FCA) based on theoretical calculations and electrical properties. The NTO thin film with a high degree of (004) orientation showed better photocatalytic performance than others due to its better absorption, more effective charge transfer, and greater ability to completely degrade pollutants. In addition, a synergistic effect for the enhancement of photocatalytic performance was observed when the thin films were irradiated by alternating the wavelength of the LED light source between 365 nm and 515 nm. We have also demonstrated that these thin films are suitable for self-cleaning coatings.

## 1. Introduction

With the development of industrialization, environmental pollution has become a major problem. Many researchers have focused on the study of environmental remediation technologies and environmentally friendly materials.[1–3] Titanium dioxide ($TiO_2$) has attracted significant attention for photocatalytic applications due to its outstanding performance, rich abundance, low cost, high stability, and environmentally friendly features.[4–8] However, due its wide band gap (~3.20 eV), it is only sensitive to ultraviolet (UV) light, which accounts for less than 5% of solar energy.

To utilize visible (vis) light for the photocatalytic application of $TiO_2$, many efforts, such as impurity doping,[9–13] construction of heterojunctions,[14,15] and localized surface plasmon resonance (LSPR) using noble metals,[6,16] have been made. Although these approaches are effective towards creating visible-light-sensitive $TiO_2$, they suffer from a limited enhancement in light absorption or high cost. Hence, it is still a great challenge to make $TiO_2$ absorb the whole spectrum of sunlight.

Niobium-doping (Nb-doping) is widely used to improve photocatalytic activities of anatase $TiO_2$, because the dopant could change the crystal structure, electrical properties, and absorption characteristics of $TiO_2$.[17–25] First, Nb-doping will induce structural evolution from rutile to anatase and improve the photocatalytic activity of $TiO_2$.[19] Second, the pentavalent niobium ion ($Nb^{5+}$) doping into $TiO_2$ introduces more electrons in the conduction band. These excess electrons can assist the speedy initial reaction of the organic decomposition process.[22,23] In addition, Nb-doping has been reported to narrow the band gap and make $TiO_2$ visible-light-sensitive due to the formation of some shallow donor or defect levels below the conduction band edge.[17,20] However, to the best of our knowledge, Nb-doped $TiO_2$ ($Nb:TiO_2$, NTO) has not been reported to absorb the whole spectrum of visible light.

Recently, in our previous study, an NTO film with a high degree of (004) orientation has been reported to exhibit conductive properties with decreased visible transmittance.[26] It is also a potential candidate as an effective photocatalyst.[21] The thin film can create a beneficial way to improve the photocatalytic performance from two aspects. On the one hand, the high percentage of exposed (001) facets will enhance the photocatalytic activity of $TiO_2$.[15,18,27] On the other hand, the decreased visible transmittance provides a novel way to use the whole spectrum of visible light for photocatalysis. In addition, the good photocatalytic performance can make the thin film interesting and attractive for self-cleaning coating applications.

---

*School of Advanced Materials, Peking University Shenzhen Graduate School, 2199 Lishui Road, Shenzhen 518055, P. R. China. E-mail: meizw@pkusz.edu.cn, panfeng@pkusz.edu.cn; Tel: +86 755 26033200*

† Electronic supplementary information (ESI) available: Simulated calculation of electronic structure, Rietveld refinement, full EDS data, XPS spectra, AFM height images and additional photocatalytic degradation figures of $TiO_2$ and NTO thin films. See DOI: 10.1039/c7cy02614e

Published on 26 January 2018. Downloaded by University Town Library of Shenzhen on 3/16/2026 1:55:49 AM.

In this study, we demonstrate that conductive thin films based on anatase NTO can increase the photocatalytic activity of anatase $TiO_2$ due to the extended free-carrier absorption (FCA) of visible-light and efficient charge transfer. The origin of FCA was studied using theoretical calculations of the electronic structure and electrical measurements and demonstrated by the UV-vis absorption spectra of $TiO_2$ and NTO. In addition, the photocatalytic activity was affected by the crystal structure of NTO. The NTO thin film with a high degree of (004) orientation shows better photocatalytic performance than others due to its better absorption, more effective charge transfer, and greater ability to completely degrade pollutants. Furthermore, a synergistic effect for the photocatalytic performance was observed for the thin film when alternating irradiation under 365 nm and 515 nm LED light was used. The application as self-cleaning coatings is also demonstrated by investigating the wettability of these thin films.

## 2. Experimental

### 2.1 General film preparation

$TiO_2$ and NTO thin films with random orientation ($TiO_2$-RO, NTO-RO) and a high degree of (004) orientation ($TiO_2$-004, NTO-004) were deposited by adjusting the sputtering angles of DC magnetron sputtering. The $TiO_2$ and NTO thin films were sputtered onto 3 × 3 $cm^2$ soda-lime glass substrates (GULUO GLASS) using an oxide target ($\Phi$6 cm). The $TiO_2$ thin film was prepared from a pure $TiO_2$ target. The NTO thin film was prepared from a $TiO_2$ target with 5 at% of the Nb dopant ($Ti_{0.95}Nb_{0.05}O_2$, 99.9%, Hzamtarget). The substrate was secured onto a 6 × 6 $cm^2$ piece of stainless steel substrate holder with a high-temperature polyamide tape (2 mm wide). The distance was 8 cm between the center of the target and the substrate. The base pressure prior to each deposition was $8 \times 10^{-4}$ Pa. The films were deposited in pure argon (grade 5.0) at a flow rate of 20 sccm (cubic centimeter per minute at STP) and a system pressure of 0.3 Pa. In addition, the substrate temperature during the deposition was 40–60 °C, measured using a thermocouple during the deposition process. A DC sputtering power (SKY Technology Development DC power system) of 40–45 W was required to prepare films with a thickness of ~350 nm on the soda-lime glass substrate after 1 h of deposition. Before each deposition, the target surface was sputter-cleaned using pure Ar for 10 min and then presputtered for 5 min under the film deposition conditions. The as-deposited films were annealed and crystallized under a $Ar/H_2$ (95 : 5, v/v) atmosphere at a flow rate of 30 sccm in a horizontal furnace at 450 °C for 30 min. The temperature was increased at a rate of 10 °C $min^{-1}$. Then, the films were naturally cooled down to room temperature.

### 2.2 Film analysis

The crystal structures of the NTO and $TiO_2$ films were analyzed using a Bruker D8 Advance powder X-ray diffractometer (XRD) equipped with Cu K$\alpha$ radiation with a two-dimensional detector. The scan range of $2\theta$ was from 10 to 120°, and the scan step of $2\theta$ was 0.02°. The scan time was 1 s per step and 2 s per step for normal analysis and Rietveld refinement, respectively.

The electrical properties of the films were measured at room temperature using an Ecopia HMS-3000 Hall effect measurement system set up in the Van der Pauw configuration. The measurements were carried out on 1 × 1 $cm^2$ squares, and the standard ITO sample was tested prior to any NTO thin film measurements.

Photoelectron spectroscopy studies were performed using a Thermo Fisher ESCALAB 250X surface analysis system equipped with a monochromatized Al anode X-ray source (X-ray photoelectron spectroscopy, XPS, $h\nu = 1486.6$ eV).

The optical properties were analyzed over the wavelength range of 300–800 nm using a Shimadzu UV-2450 spectrometer with an integrating sphere. The standard sample was newly prepared using anhydrous $BaSO_4$ powder.

The photoluminescence (PL) spectra were measured using a Perkin Elmer LS 55 Fluorescence spectrometer with a thin film carrier.

The morphologies of the thin films were measured using the Zeiss SUPRA-55 scanning electron microscope (SEM).

The content of Nb was investigated *via* an Oxford-Max 20 energy dispersive spectrometer (EDS).

The surface morphology, roughness, and specific area of thin films were measured and analyzed by the Bruker MultiMode 8 AFM (atomic force microscope) using a tapping model with SCM-PIT probes.

The thin films were characterized using Raman spectroscopy with the laser excitation energy of 532 nm using a Horiba iHR320 Raman spectrometer with a cooled CCD detector.

The thickness of the films was measured using a Bruker DektakXT profilometer with a proper measurement range of 6.5 μm.

The static contact angles (CAs) were measured using a goniometer (250-F1, Dongguan Precise Test Equipment Co., Ltd). Droplets of distilled water with a volume of 5 μL were placed gently onto the surface at room temperature and pressure. The static CAs of the thin films were measured three times at different locations such that the measurement variance was ±2°.

Images were obtained using the camera of a Huawei Mate 8 mobile phone.

### 2.3 The degree of preferential (004) orientation ($\eta_{(004)}$)

The degree of preferential (004) orientation can be quantified as follows:

$$\eta_{(004)} = \sqrt{\frac{\left(1 - \mathrm{MD}_{(004)}\right)^3}{1 - \mathrm{MD}_{(004)}{}^3}} \times 100\% \tag{1}$$

where $\mathrm{MD}_{(004)}$ is the March–Dollase parameter for the (004) direction, which can be obtained from the Rietveld refinement.[28]

This journal is © The Royal Society of Chemistry 2018

Published on 26 January 2018. Downloaded by University Town Library of Shenzhen on 3/16/2026 1:55:49 AM.

### 2.4 Catalytic activity tests

**Photocatalytic degradation of rhodamine B (RhB) under simulated solar light irradiation.**[29] Annealed $TiO_2$ and the NTO thin films were cleaned by ultrasonic treatment in a detergent, deionized water, acetone, and isopropyl alcohol for 10 min each and subsequently dried under a flow of $N_2$. An ethanol solution of RhB at 10 000 ppm was prepared for the dye degradation experiment. Subsequently, the prepared solution was spin-coated onto the NTO thin film surface at 600 rpm for 30 seconds. The as-prepared samples were stored in a glass dish covered with an Al foil. After being allowed to dry naturally, the samples were kept on a plate at a constant temperature of 25 °C and evaluated for photocatalytic activity by monitoring the decolorization of RhB under an AM 1.5 illumination *via* an ABET sun 3000 solar simulator. The power of the light was calibrated to one sun light intensity using an NREL-calibrated Si cell (Oriel 91150). After a specified time, the maximum peak of the absorbance band was monitored using a UV-vis spectrophotometer (Shimadzu UV-2450) to estimate the amount of RhB. According to the Lambert–Beer law, the absorbance is proportional to the concentration of a dilute solution, and the degradation of RhB can be described as follows:

$$\ln\frac{C_0}{C} = kt \tag{2}$$

where $C_0$ is the initial concentration of the RhB solution, $C$ is the concentration at a specified irradiation time, $k$ is the reaction rate, and $t$ is the reaction time. We suppose that this law can be applied to RhB molecules on the surface of thin films.

**2.4.1. Photocatalytic degradation of RhB under single-wavelength LED irradiation.** An ethanol solution of RhB at 120 ppm was prepared for the dye degradation experiment. Then, 2 mL of the abovementioned solution was added to a 10 mL glass bottle. The as-prepared thin film was placed into the solution and left for about 20 min. About 1 mL of the solution was transferred into a quartz colorimetric utensil and then measured. Subsequently, the maximum peak of the absorbance band was monitored to estimate the amount of RhB, and the solution was then transferred back to the glass bottle. Then, the thin film was irradiated under a single-wavelength LED point light source (SZLAMPLIC, $\Phi 3$ mm) with a 1 × 1 $cm^2$ light spot. The power of the light was measured using a normal light meter (CEAULIGHT, CEL-NP2000). After a specified time, the maximum peak of the absorbance band was monitored using a UV-vis spectrophotometer to estimate the amount of RhB.

## 3. Results and discussion

### 3.1 The origin of the whole visible absorption

The optical properties of a material are mainly related to its electronic structure.[30] The electronic structures of pure $TiO_2$ and $Nb:TiO_2$ (5 : 95, at%) with an anatase structure were calculated using the Vienna *ab initio* simulation package (VASP) based on a generalized gradient approximation with Hubbard U correction (GGA+U) to the density functional theory (DFT). The Fermi level of pure $TiO_2$ is between the conduction and valence band; this indicates no free electrons in the undoped $TiO_2$ (Fig. 1a and b). Therefore, pure $TiO_2$ only shows intrinsic UV absorption. After Nb doping, the Fermi level moves into the conduction band (Fig. 1c and d). There are d-orbital electrons of both Ti and Nb in the conduction band (Fig. 1d). In other words, NTO has free electrons and thus exhibits good conductivity.

The existence of free electrons in the conduction band of NTO was also confirmed by the electrical properties of the NTO thin films. The electrical properties were characterized using the standard four-probe Hall effect measurements. As listed in Table 1, both NTO-RO (random orientation) and NTO-004 (high degree of (004) orientation) show good conductivity with a low resistivity (in the order of $10^{-4}$ Ω cm), whereas $TiO_2$ shows very high resistivity such that it cannot be measured using the Hall effect measurements or a two-

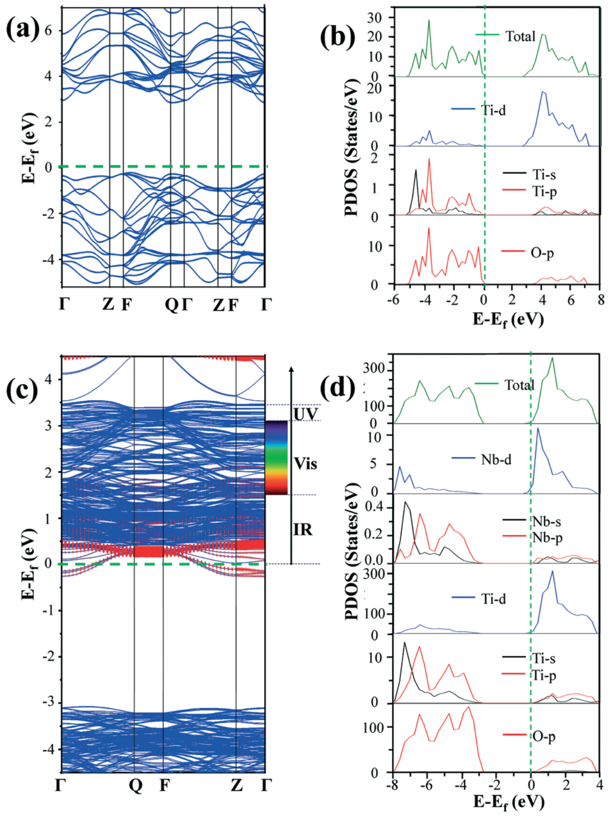

**Fig. 1** (a) The electronic band structure of pure $TiO_2$. (b) PDOS (DOS on specified atoms and orbitals) of pure $TiO_2$ at the DFT level. (c) The electronic band structure of $Nb:TiO_2$ (5% of Nb dopant). The blue lines represent the band structure of the $Nb:TiO_2$ system. The red dots represent the band structures of Nb. The dot size is proportional to the weight. The green dashed lines represent the Fermi level. The spectra card on the right shows the reference of UV-vis-IR free-carrier absorption. (d) Projected density of states (PDOS) (DOS on specified atoms and orbitals) of $Nb:TiO_2$ at the DFT level. The Fermi level is at zero energy and marked by the green dashed line.

Published on 26 January 2018. Downloaded by University Town Library of Shenzhen on 3/16/2026 1:55:49 AM.

**Table 1** Electrical properties of the NTO thin films

| Sample | Sheet resistance [Ω sq$^{-1}$] | $\rho$ [Ω cm] | $N$ [cm$^{-3}$] | $\mu$ [cm$^2$ V$^{-1}$ s$^{-1}$] |
|---|---|---|---|---|
| NTO-RO | 26.5 | $9.4 \times 10^{-4}$ | $2.21 \times 10^{21}$ | 3.01 |
| NTO-004 | 18.6 | $6.6 \times 10^{-4}$ | $2.13 \times 10^{21}$ | 4.44 |
| $TiO_2$ | [a] | [a] | [a] | [a] |

[a] The resistivity of $TiO_2$-RO and $TiO_2$-004 is very high such that it cannot be measured using the Hall effect measurements or a two-point probe of Agilent Millimeter.

point probe of Agilent millimeter. In addition, the Hall effect measurements indicated that the NTO films displayed n-type conductivity, with electrons being the dominant charge carrier species. These results also confirm that the Fermi level of NTO moves into the conduction band.

After Nb doping, the energy levels of NTO become degenerate. The degenerate energy levels of NTO make direct FCA available because the conduction-band states are available in the UV-vis-IR energy range to accommodate the free electrons excited by the vertical transitions (Fig. 1c).[31–33] Hence, both the intrinsic UV absorption and UV-vis-IR FCA can occur in NTO. This result is in contrast to that observed for the tin dioxide ($SnO_2$) TCO thin films reported by H. Peelaers,[34] but is in good agreement with that observed for the NTO thin films calculated by R. S. Zhang.[30]

Normally, the FCA is too weak to influence the properties of a semiconductor; however, the FCA becomes significant at high carrier concentrations (in the order of $10^{20}$–$10^{21}$ cm$^{-3}$).[32,34] The carrier concentrations of the NTO thin films are in the order of $10^{21}$ cm$^{-3}$ (Table 1); thus, the FCA should not be negligible for conductive NTO thin films.

Based on the abovementioned theoretical calculation and experimental electrical measurement analysis, we consider that the conductive NTO thin films can absorb the whole spectrum of visible light due to their electronic structure. On the one hand, there are abundant free electrons in the conduction band of NTO. On the other hand, the energy levels of NTO are degenerate, and their conduction-band states are available for free electron excitation.

### 3.2 The preparation, identification, and morphology of the thin films

To further study the photocatalytic activities and optional properties of NTO, both the NTO (with 5 at% of the Nb dopant) and pure $TiO_2$ thin films were prepared with random orientation (NTO-RO, $TiO_2$-RO) and a high degree of (004) orientation (NTO-004, $TiO_2$-004) using our reported method.[26]

A systematic XRD study shows that both the $TiO_2$ and NTO thin films exhibit a typical anatase phase (Fig. 2a). There are no diffraction peaks observed for the rutile or brookite phases. The peaks centred around 25.23° and 37.78° can be ascribed to the (101) and (004) facets of anatase $TiO_2$, respectively. The (101) peaks are stronger than the (004) peaks observed for the thin films with random orientation, whereas the opposite results have been observed for the thin film with a high degree of (004) orientation. Compared with the anatase phase of pure $TiO_2$, the XRD peak position of the NTO thin films presents a little shift towards the low angle region. This is attributed to the doping effect of Nb because the ionic radius of $Nb^{5+}$ (*ca.* 0.70 Å) is slightly larger than that of $Ti^{4+}$ (*ca.* 0.68 Å).

The Le Bail analysis was used to fit the XRD patterns with TOPAS to obtain the unit cell parameters, unit volume, and March–Dollase parameters obtained for the (004) direction (Fig. S1 in the ESI†). The unit cell parameters are $a$ = 3.786 Å and $c$ = 9.504 Å for the pure $TiO_2$ thin films (Table S1 in ESI†). After Nb doping, both $a$ and $c$ increase around 3.810 Å and 9.540 Å, respectively. The March–Dollase (MD) parameters were fitted to be 0.722, 0.558, 0.787, and 0.482 for the thin films of $TiO_2$-RO, $TiO_2$-004, NTO-RO, and NTO-004, respectively. Therefore, the degree of the preferential (004) orientation was quantified to be 18.6%, 32.3%, 13.7%, and 39.6% for thin films of $TiO_2$-RO, $TiO_2$-004, NTO-RO, and NTO-004, respectively (Table 2). The EDS data of $TiO_2$ and NTO thin films on soda-lime glass reveal the content of Nb and Ti as listed in Table S2 in the ESI† (the details are shown in Fig. S2 in the ESI†). Nb was undetected in pure $TiO_2$. The doping content of Nb was 8.6 at% and 8.3 at% in the NTO-RO and NTO-004 samples, respectively. The difference in the Nb-doping content between the thin film and the target is because the sputtering yield of Nb atom is slightly higher than that of the Ti atom.

The typical Raman spectra of the $TiO_2$ and NTO thin films located between 100 and 700 cm$^{-1}$ (Fig. 2b). Compared with pure $TiO_2$, the $E_g$ mode (around 144 cm$^{-1}$) of NTO exhibits a

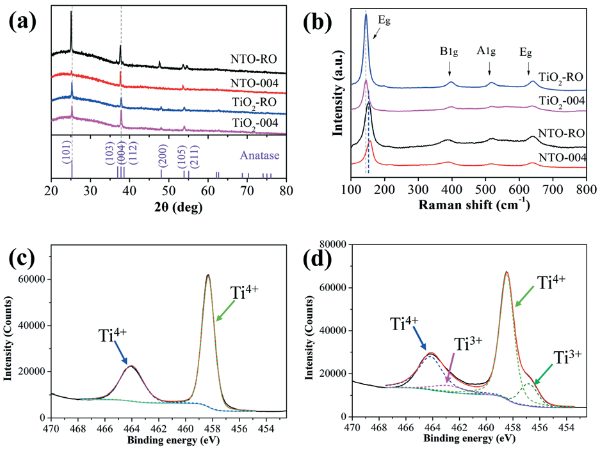

**Fig. 2** (a) The XRD patterns of the anatase $TiO_2$ and NTO thin films with random orientation (NTO-RO, $TiO_2$-RO) and a high degree of (004) orientation (NTO-004, $TiO_2$-004). (b) The Raman spectra obtained for the anatase $TiO_2$-RO, $TiO_2$-004, NTO-RO, and NTO-004 thin films. (c) The XPS spectra obtained for the pure $TiO_2$ thin films showing the $Ti^{4+}$ state only for the $2p_{3/2}$ transition. (d) The XPS spectra obtained for the NTO thin films showing the $Ti^{4+}$ and $Ti^{3+}$ states for the $2p_{3/2}$ transition. The data was treated with a Shirley background and individual Gaussian/Lorentzian functions for the $Ti^{4+}$ and $Ti^{3+}$ final states.

This journal is © The Royal Society of Chemistry 2018

Published on 26 January 2018. Downloaded by University Town Library of Shenzhen on 3/16/2026 1:55:49 AM.

Table 2 Electrical properties of the NTO thin films

| Sample | MD | $\eta$(004) (%) | Band gap (eV) | Surface roughness, $R_q$ (nm) | Surface area ($\mu m^2$) |
|---|---|---|---|---|---|
| $TiO_2$-RO | 0.722 | 18.6 | 3.34 | 3.57 | 1.03 |
| $TiO_2$-004 | 0.558 | 32.3 | 3.29 | 3.49 | 1.07 |
| NTO-RO | 0.787 | 13.7 | 3.43 | 1.11 | 1.03 |
| NTO-004 | 0.482 | 39.6 | 3.38 | 2.57 | 1.06 |

blue shift. In addition, as the (004)-oriented growth becomes stronger, the $E_g$ mode (around 144 $cm^{-1}$) of NTO is further blue shifted. This result was in good agreement with our previously reported results.[26] The XRD patterns and Raman spectra indicate that the anatase thin films are successfully prepared with random orientation and a high degree of (004) orientation, respectively.

X-ray photoelectron spectroscopy (XPS) was employed to observe the doping of niobium. No Nb could be detected by XPS measurement in the pure $TiO_2$ sample. As shown in Fig. 2c, the $Ti^{4+}$ peaks with the binding energy (BE) of 458.3 and 464.0 eV were well fitted with the XPS spectra observed for the Ti $2p_{3/2}$ and Ti $2p_{1/2}$ transitions, respectively, of pure $TiO_2$. After Nb doping, the $Ti^{4+}$ peaks with the BE of 458.5 and 464.2 eV for the Ti $2p_{3/2}$ and Ti $2p_{1/2}$ transitions, respectively, become predominant. However, the reduced titanium state ($Ti^{3+}$) peaks with the BE of 456.8 and 462.8 eV were observed because of the compensating mechanism of the redundant electrons of Nb.[35] The reduced titanium state gives some asymmetry to the Ti $2p_{3/2}$ and Ti $2p_{1/2}$ transitions of NTO. The thin films with random orientation and a high degree of (004) orientation show similar XPS results (Fig. S3 in the ESI†). These results indicate the formation of the $Ti^{3+}$ state and the successful doping of Nb.

Scanning electron microscopy (SEM) and atomic force microscopy (AFM) images were employed to study the morphology of the thin films. As shown in Fig. 3, the surface morphologies are different between pure and the Nb-doped $TiO_2$ thin films. The small particles are spread over the surface of the pure $TiO_2$ thin films (Fig. 3a and c), whereas some larger particles can be seen on the surface of the NTO thin films (Fig. 3e and g). The side-on images show that the thickness of the thin films is ~350 nm. AFM was performed on all positions in 1 μm × 1 μm areas of the NTO and $TiO_2$ thin films (Fig. S4 in the ESI†). The root-mean-square roughnesses ($R_q$) are 3.57, 3.49, 1.11, and 2.57 nm for the $TiO_2$-RO, $TiO_2$-004, NTO-RO, and NTO-004 thin films, respectively. These results indicate that the NTO and $TiO_2$ thin films are compact and smooth (Fig. 3a–h). However, the calculated surface areas are different and measured to be 1.03, 1.07, 1.03, and 1.06 $\mu m^2$ for the $TiO_2$-RO, $TiO_2$-004, NTO-RO, and NTO-004 thin films, respectively. The AFM 3D images show that the particles are cone-shaped on the surface of the $TiO_2$ and NTO thin films (Fig. 3). The NTO thin films show more sharply cone-shaped particles than those observed in pure $TiO_2$. Moreover, the distribution of the cone-shaped particles is denser on the surface of the thin films with a high degree of (004) orientation than that on the thin films with random orientation.

### 3.3 The electrical and optical properties of the thin films

The electrical properties of the NTO thin films are listed in Table 1. Both NTO-RO and NTO-004 show good conductivity with the carrier concentrations >2 × $10^{21}$ $cm^{-3}$. The NTO-004 thin film shows better conductivity than NTO-RO due to the increase in the Hall mobility.[26] The sheet resistances are as low as 26.5 and 18.6 Ω $sq^{-1}$ for the NTO-RO and NTO-004 thin films, respectively. However, the resistivity of the $TiO_2$ thin films was too high to be measured. The electrical properties of the NTO and $TiO_2$ thin films indicate that the free

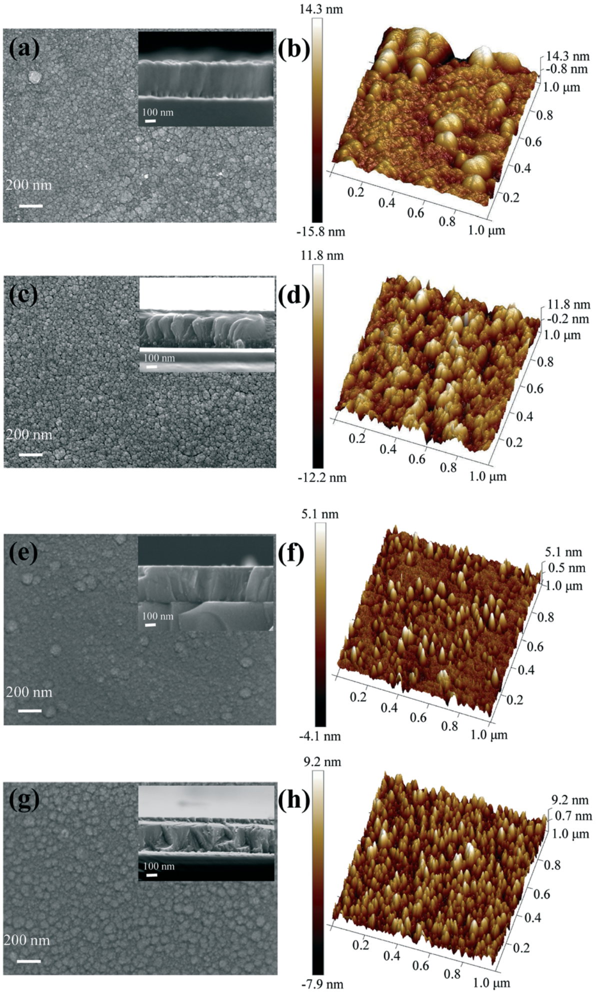

Fig. 3 The top-down SEM images and AFM 3D images of the thin films of $TiO_2$-RO (a and b), $TiO_2$-004 (c and d), NTO-RO (e and f), and NTO-004 (g and h). The insets of SEM images depict side-on images of thin films.

Published on 26 January 2018. Downloaded by University Town Library of Shenzhen on 3/16/2026 1:55:49 AM.

electrons are in high concentration in the NTO samples but are not observed in $TiO_2$. This result makes UV-vis-IR FCA occur in the NTO thin films.

The UV-vis absorbance spectra of NTO-RO, NTO-004, $TiO_2$-RO, and $TiO_2$-004 were converted from reflectance to absorbance using the Kubelka–Munk method (Fig. 4a and b). Compared with pure $TiO_2$, the NTO thin films show better absorption properties in the region of 550–800 nm; this indicates that Nb-doping significantly modifies the visible light absorption characteristics of $TiO_2$. This result was in good agreement with our analysis of the simulated calculations. Moreover, the absorption properties of the random orientation and high degree of (004) orientation samples show a slight difference because of the anisotropy of the dielectric function observed for $TiO_2$ along the different crystal orientations.[36] Based on the abovementioned analysis, NTO with both a random orientation (NTO-RO) and a high degree of (004) orientation (NTO-004) can absorb the whole spectrum of visible light.

In Fig. 4c, the intrinsic optical band gaps of the $TiO_2$ and NTO thin films are shown by constructing Tauc plots using the $(\alpha h\nu)^{1/2}$ relation. The values of Tauc's gap ($E_g$) were evaluated from the extrapolation of the high energy points to intercept on the energy axis with little absorption. The indirect band gaps were determined to be 3.43, 3.38, 3.34, and 3.29 eV for the NTO-RO, NTO-004, $TiO_2$-RO, and $TiO_2$-004 thin films, respectively. After Nb doping, an obvious blue shift was found for the intrinsic UV absorption edge of the conductive NTO thin films. This result can be rationalized by the Burstein–Moss effect, which increases the optical band gap as electrons populate the conduction band.[26,37] This result is different from the effect of Nb-doping in non-conductive Nb-doped $TiO_2$ powder. Narrowed band gaps were observed because of the formation of some shallow donor or defect levels below the conduction band edge.[17,20] This result also confirms that the Fermi level of NTO moves into the conduction band.

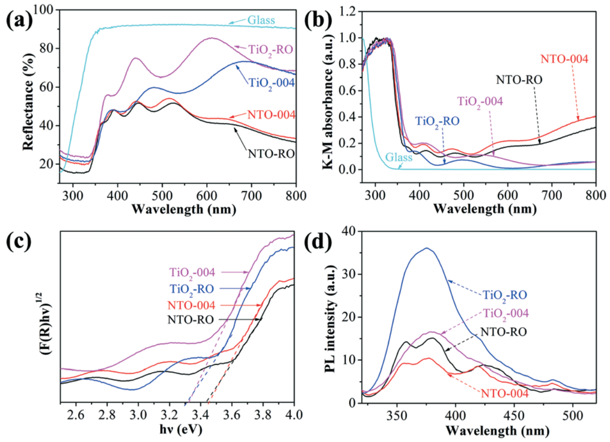

**Fig. 4** (a) The diffuse reflectance spectra obtained for the $TiO_2$-RO, $TiO_2$-004, NTO-RO, and NTO-004 thin films and glass substrate. (b) The absorption spectra of the thin films and glass substrate converted from DRS using the Kubelka–Munk function. (c) The intrinsic optical absorption edges (eV) obtained for the thin films. (d) The photoluminescence (PL) spectra obtained for the thin films with laser excitation at 300 nm.

Fig. 4d shows the photoluminescence (PL) spectra of the $TiO_2$-RO, $TiO_2$-004, NTO-RO, and NTO-004 thin films under 300 nm laser excitation. After Nb doping, there are two more emission centers than pure $TiO_2$, which result from the change in the energy bands. The emission peaks around 360 (3.4 eV), 380 (3.3 eV), and 430 (2.9 eV) nm were attributed to the radiative recombination of electrons in the super-band-gap states, shallow complex $(Nb_{Ti}–V_{Ti})^{3-}$ states, and $O_i^{2-}$ states with holes in the valence band, respectively.[17] The emission peaks around 480 nm (2.55 eV) were attributed to the radiative recombination of electrons in the super-band-gap states with holes in the surface peroxo states.[20] However, the general trend in the photoluminescence spectra intensity was $TiO_2$-RO > $TiO_2$-004 > NTO-RO > NTO-004. This indicates that Nb doping can decrease the PL intensity. The NTO-004 thin film shows the lowest radiative recombination of photoexcited electron–hole pairs. There are three reasons for the improvement in the charge separation observed for NTO-004. First, the introduction of $Nb^{5+}$ into the $TiO_2$ structure can improve the conductivity, as shown in Table 1. This facilitates the migration of photoexcited electrons to the NTO surface and suppresses their recombination. Second, the charge mobility becomes higher because the static effective mass $m^*$ along the $a$ axis ($m_{(100)}^*$) is lesser than that along the $c$ axis ($m_{(001)}^*$).[38] Third, the transfer and separation of the photogenerated charges can be enhanced when the percentage of (004) facets increases.[15]

### 3.4 The photocatalytic abilities of the thin films

The photocatalytic abilities of the NTO and $TiO_2$ thin films were demonstrated by degrading the surface-coated RhB (Fig. S5 in the ESI†). RhB is a carcinogenic compound, which is often chosen as a model molecule for photocatalytic degradation. Both the NTO and $TiO_2$ thin films show good photocatalytic ability under simulated AM 1.5 solar light irradiation ($100\ mW\ cm^{-2}$) at a constant temperature of 25 °C (Fig. 5a). However, the photocatalytic abilities observed between the NTO and $TiO_2$ thin films were different (Fig. 5a and b). The trend in the photocatalytic ability was NTO-004 > NTO-RO > $TiO_2$-004 > $TiO_2$-RO. The NTO-004 thin films show better photocatalytic performance than others because of its better light absorption and lower radiative recombination. After 2 h of irradiation, about 70% of RhB was degraded using the NTO-004 thin film.

The photocatalytic activity depends on the surface morphology of the thin films. The trend of the calculated surface area is $TiO_2$-004 > NTO-004 > $TiO_2$-RO = NTO-RO. Obviously, the thin films with a high degree of (004) orientation have a larger contact area than those with a random orientation. Therefore, both the $TiO_2$ and NTO thin films with a high degree of (004) orientation show better photocatalytic performance than those with a random orientation. However, the

This journal is © The Royal Society of Chemistry 2018

Published on 26 January 2018. Downloaded by University Town Library of Shenzhen on 3/16/2026 1:55:49 AM.

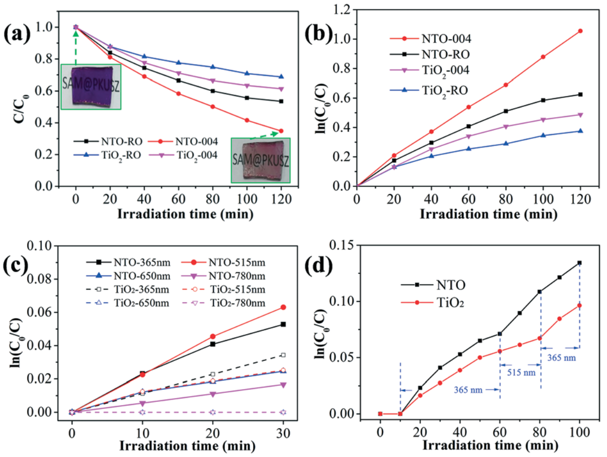

**Fig. 5** (a) A comparison of the photocatalytic degradation rates obtained for Rh B using the NTO and $TiO_2$ thin films. The optical images show the initial and final states under simulated solar light irradiation. (b) The reaction rates ($k$-value) obtained for the photocatalytic degradation process using the NTO and $TiO_2$ thin films. (c) The reaction rates obtained for the photocatalytic degradation process using the NTO and $TiO_2$ thin films under different irradiation wavelengths. The lines of the results obtained for NTO-650 nm and $TiO_2$-515 nm are almost identical. The lines of the results obtained for $TiO_2$-650 nm and $TiO_2$-780 nm are identical. (d) The reaction rates of photocatalytic degradation for NTO and $TiO_2$ thin films under 365 and 515 nm irradiations. The films are without light irradiation for an initial 10 min period.

$TiO_2$-004 thin film shows a poorer photocatalytic performance than NTO-RO although it has a larger specific area than NTO-RO. This result was because NTO-RO could absorb the whole spectrum of visible light, whereas $TiO_2$-004 was unable to do so.

Fig. 5b shows the reaction rates ($k$-value) of photocatalytic degradation for NTO and $TiO_2$ thin films. Only the NTO-004 thin film was found to have a constant reaction rate because RhB could be completely and quickly degraded using the NTO-004 thin film. The gradually decreasing reaction rates obtained for the other thin films were caused by the incomplete degradation of RhB or poor photocatalytic ability. The complete and incomplete degradation of RhB can be identified by the variation in the absorption spectra.[39] The absorption peaks of RhB gradually decrease; this suggests cleavage of the whole chromophore structure of RhB, namely complete degradation, *e.g.* the case of the thin films with a high degree of 004 orientation (Fig. S5b and d in the ESI†); when only *N*-de-ethylation occurs, RhB is incompletely degraded, and the absorption maximum is gradually blue-shifted, *e.g.* the case of the thin films with random orientation (Fig. S5a and c in the ESI†). Therefore, the complete degradation of RhB is of importance for photocatalytic reactions.

The photocatalytic abilities of the NTO-004 and $TiO_2$-004 thin films were also demonstrated by degrading RhB under a single-wavelength LED irradiation. To avoid the intrinsic absorption of the thin films, 365 (45.6 mW $cm^{-2}$), 515 (45.8 mW $cm^{-2}$), 650 (100 mW $cm^{-2}$), and 780 nm (100 mW $cm^{-2}$) LED irradiations were used (Fig. S6 in the ESI†). The NTO-004 thin film was active for photocatalysis under these wavelengths of irradiation; this indicated that the corresponding FCA was implemented in the NTO-004 thin film. There were no free electrons in the $TiO_2$ thin film, and as a result, it was only active under 365 and 515 nm irradiations (Fig. 5c). This result was in good agreement with our absorbance spectra analysis results.

Amazingly, the NTO-004 thin film shows better performance under 515 nm of LED irradiation than that under 365 nm, whereas the $TiO_2$-004 thin films show the opposite performance (Fig. 5c). This result was because the 515-nm irradiation light could be absorbed by both the thin film and RhB (Fig. S7 in the ESI†). After being excited, RhB can inject electrons into the conduction bands of both $TiO_2$-004 and NTO-004.[40,41] However, only the electrons injected into NTO-004 can be quickly transported and reused because the NTO-004 thin film has good conductive properties.[42] The electrons injected into $TiO_2$-004 are of non-effective utilization. This result indicates that RhB can be photodegraded by the NTO-004 thin film although the incident light is blocked by the surface-coated dyes. This conclusion has been confirmed by an additional experiment, as shown in Fig. 6. Both NTO-RO and NTO-004 show good photocatalytic activity when the incident light is from the RhB coating surface.

It should be noticed that the reaction rates obtained for NTO-004 gradually decrease under both 365 and 515 nm LED light source irradiations (Fig. 5c). This result seems to be in conflict with that obtained under solar light irradiation (Fig. 5b). To make this clear, 365 and 515 nm LED light source irradiations are used interchangeably for photocatalytic degradation. The reaction rates of both NTO and $TiO_2$ gradually decreased under 365 nm irradiation (Fig. 5d). However, after 515 nm irradiation, the reaction rates of all the thin films were increased under the latter 365 nm irradiation.

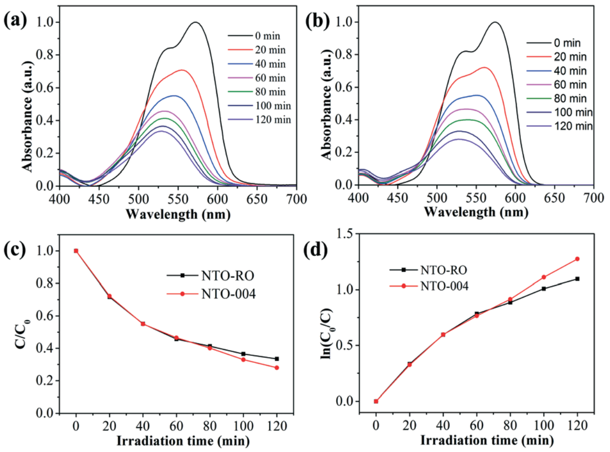

**Fig. 6** The variation in the absorption spectra of surface-coated RhB degraded using NTO-RO (a) and NTO-004 (b) under simulated solar light irradiation. (c) A comparison of the photocatalytic degradation rates obtained for RhB using the NTO-RO and NTO-004 thin films. (d) The reaction rates ($k$-value) obtained for the photocatalytic degradation using the NTO-RO and NTO-004 thin films. The incident light is from the RhB coating surface in these tests.

Published on 26 January 2018. Downloaded by University Town Library of Shenzhen on 3/16/2026 1:55:49 AM.

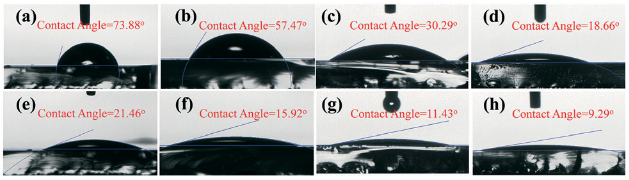

**Fig. 7** The contact angles and optical images obtained for the as-prepared (a)–(d) and UV-treated (e–h) NTO and $TiO_2$ thin films. From left to right: $TiO_2$-RO, $TiO_2$-004, NTO-RO, and NTO-004 thin films.

This result indicates that there may be a synergistic effect for the photocatalytic performance when the thin films are alternately irradiated under 365 nm and 515 nm LED.

### 3.5 Self-cleaning performance

A self-cleaning coating can remove pollutants and stains on its surface and saves a lot of time and cost for the maintenance of buildings, cars, outdoor facilities, and solar panels.[43–48] For application as self-cleaning coatings, the thin films should be hydrophobic or hydrophilic. $TiO_2$ and NTO thin films have photo-induced hydrophilicity.[46–48] However, some adsorbates are not removed completely on both hydrophobic and hydrophilic surfaces if rainwater is not abundant or energetic. Photocatalysts can transform the residuals into harmless small molecules and remove them in a simple way upon being exposed to sunlight. The combination of photocatalytic and hydrophilic properties makes a self-cleaning coating effective on both rainy and sunny days.

The wettability of both the $TiO_2$ and NTO thin films was investigated by their contact angles. The contact angles were 73.88°, 57.47°, 30.29°, and 18.66° for the $TiO_2$-RO, $TiO_2$-004, NTO-RO, and NTO-004 thin films, respectively (Fig. 7a–d). After UV irradiation, the contact angles are decreased to 21.46°, 15.92°, 11.43°, and 9.29° (Fig. 7e–h). All the thin films show good hydrophilic properties and are suitable as self-cleaning coatings. The wettability is commonly related to the surface nanostructure of the thin films. Compared with pure $TiO_2$ thin film, the particles are more sharply cone-shaped on the surface of the NTO thin films (Fig. 3). Therefore, the NTO thin films show better wettability than the $TiO_2$ thin films. Moreover, the cone-shaped particles are distributed more densely on the surface of NTO-004 than that on the surface of NTO-RO; thus, NTO-004 shows better hydrophilic properties than others. These results indicate that the NTO thin films can act as an effective self-cleaning coating for the glass.

## Conclusions

In summary, we have demonstrated a novel way to utilize the whole spectrum of visible light to improve the photocatalytic performance. After Nb doping, the energy levels of $TiO_2$ are degenerate, and the corresponding carrier concentrations of the thin films are in the order of $10^{21}$ $cm^{-3}$. These two aspects make the NTO thin films absorb the whole spectrum of visible light. The absorption of the whole spectrum of visible light was demonstrated using theoretical calculations, absorbance spectra, and electrical properties. In addition, the photocatalytic activities of the thin films were correlated with their crystal orientation, surface morphology, and photoluminescence spectra. NTO thin films with a high degree of (004) orientation show better photocatalytic performance than others due to better absorption, more effective charge transfer, and greater ability to completely degrade pollutants. In addition, a synergistic effect for the photocatalytic performance was observed when the thin films were irradiated alternatively with LED light at 365 nm and 515 nm. Finally, the combination of the photocatalytic and hydrophilic properties makes the NTO thin films suitable for self-cleaning coatings on both rainy and sunny days.

## Conflicts of interest

There are no conflicts of interest to declare.

## Acknowledgements

This work was supported by the financial support received from the Shenzhen Key Science and Technology Plan (Grant No. JSGG20141118144410953), the Guangdong Applied Technology Research Special Project (Grant No. 2015B090927003), and the Shenzhen Science and Technology Innovation Committee Grant (Grant No. JCYJ20150331101121646).

## Notes and references

1 J. Low, B. Cheng and J. Yu, *Appl. Surf. Sci.*, 2017, **392**, 658–686.
2 M. M. Khin, A. S. Nair, V. J. Babu, R. Murugan and S. Ramakrishna, *Energy Environ. Sci.*, 2012, **5**, 8075–8109.
3 M. Pelaez, N. T. Nolan, S. C. Pillai, M. K. Seery, P. Falaras, A. G. Kontos, P. S. M. Dunlop, J. W. J. Hamilton, J. A. Byrne, K. O'Shea, M. H. Entezari and D. D. Dionysiou, *Appl. Catal., B*, 2012, **125**, 331–349.
4 J. Schneider, M. Matsuoka, M. Takeuchi, J. Zhang, Y. Horiuchi, M. Anpo and D. W. Bahnemann, *Chem. Rev.*, 2014, **114**, 9919–9986.
5 J. Liu, Y. Liu, N. Liu, Y. Han, X. Zhang, H. Huang, Y. Lifshitz, S. T. Lee, J. Zhong and Z. Kang, *Science*, 2015, **347**, 970–974.
6 C. Clavero, *Nat. Photonics*, 2014, **8**, 95–103.
7 C. Wang, C. Shao, Y. Liu and X. Li, *Inorg. Chem.*, 2009, **48**, 1105–1113.
8 A. Fujishima and K. Honda, *Nature*, 1972, **238**, 37–38.
9 R. Asahi, T. Morikawa, H. Irie and T. Ohwaki, *Chem. Rev.*, 2014, **114**, 9824–9852.
10 H. Choi, D. Shin, B. C. Yeo, T. Song, S. S. Han, N. Park and S. Kim, *ACS Catal.*, 2016, **6**, 2745–2753.
11 N. Feng, Q. Wang, A. Zheng, Z. Zhang, J. Fan, S. B. Liu, J. P. Amoureux and F. Deng, *J. Am. Chem. Soc.*, 2013, **135**, 1607–1616.
12 X. Yang, C. Cao, L. Erickson, K. Hohn, R. Maghirang and K. Klabunde, *Appl. Catal., B*, 2009, **91**, 657–662.

This journal is © The Royal Society of Chemistry 2018

Published on 26 January 2018. Downloaded by University Town Library of Shenzhen on 3/16/2026 1:55:49 AM.

13 R. Asahi, T. Morikawa, T. Ohwaki, K. Aoki and Y. Taga, *Science*, 2001, **293**, 269–271.

14 X. Yue, S. Yi, R. Wang, Z. Zhang and S. Qiu, *J. Mater. Chem. A*, 2017, **5**, 10591–10598.

15 J. Yu, J. Low, W. Xiao, P. Zhou and M. Jaroniec, *J. Am. Chem. Soc.*, 2014, **136**, 8839–8842.

16 F. Mushtaq, A. Asani, M. Hoop, X. Z. Chen, D. Ahmed, B. J. Nelson and S. Pané, *Adv. Funct. Mater.*, 2016, **26**, 6995–7002.

17 S. Khan, H. Cho, D. Kim, S. S. Han, K. H. Lee, S. H. Cho, T. Song and H. Choi, *Appl. Catal., B*, 2017, **206**, 520–530.

18 L. Kong, C. Wang, F. Wan, L. Li, X. Zhang and Y. Liu, *Dalton Trans.*, 2017, **46**, 15363–15372.

19 H. Y. Wang, J. Chen, F. X. Xiao, J. Zheng and B. Liu, *J. Mater. Chem. A*, 2016, **4**, 6926–6932.

20 L. Kong, C. Wang, H. Zheng, X. Zhang and Y. Liu, *J. Phys. Chem. C*, 2015, **119**, 16623–16632.

21 D. S. Bhachu, S. Sathasivam, G. Sankar, D. O. Scanlon, G. Cibin, C. J. Carmalt, I. P. Parkin, G. W. Watson, S. M. Bawaked, A. Y. Obaid, S. Al-Thabaiti and S. N. Basahel, *Adv. Funct. Mater.*, 2014, **24**, 5075–5085.

22 B. N. Joshi, H. Yoon, M. F. A. M. V. Hest and S. S. Yoon, *J. Am. Ceram. Soc.*, 2013, **96**, 2623–2627.

23 J. Yang, X. Zhang, C. Wang, P. Sun, L. Wang, B. Xia and Y. Liu, *Solid State Sci.*, 2012, **14**, 139–144.

24 K. A. Michalow, D. Flak, A. Heel, M. Parlinska-Wojtan, M. Rekas and T. Graule, *Environ. Sci. Pollut. Res.*, 2012, **19**, 3696–3708.

25 A. Mattsson, M. Leideborg, K. Larsson, G. Westin and L. Osterlundet, *J. Phys. Chem. B*, 2006, **110**, 1210–1220.

26 X. Yang, M. J. Zhang, Y. Min, M. Xu, Z. Mei, J. Liang, J. Hu, S. Yuan, S. Xiao, Y. Duan, F. Liu, H. Lin, Y. Lin and F. Pan, *ACS Appl. Mater. Interfaces*, 2017, **9**, 29021–29029.

27 H. G. Yang, C. H. Sun, S. Z. Qiao, J. Zou, G. Liu, S. C. Smith, H. M. Cheng and G. Q. Lu, *Nature*, 2008, **453**, 638.

28 B. I. Stefanov, G. A. Niklasson, C. G. Granqvist and L. Osterlund, *J. Mater. Chem. A*, 2015, **3**, 17369–17375.

29 F. Wang, G. Zhang, Z. Zhao, H. Tan, W. Yu, X. Zhang and Z. Sun, *RSC Adv.*, 2015, **5**, 9861–9864.

30 R. S. Zhang, Y. Liu, Q. Gao, F. Teng, C. L. Song, W. Wang and G. R. Han, *J. Alloys Compd.*, 2011, **509**, 9178–9182.

31 A. Schleife, C. Rödl, F. Fuchs, K. Hannewald and F. Bechstedt, *Phys. Rev. Lett.*, 2011, **107**, 236405.

32 E. Kioupakis, P. Rinke, A. Schleife, F. Bechstedt and C. G. Van De Walle, *Phys. Rev. B: Condens. Matter Mater. Phys.*, 2010, **81**, 2–5.

33 H. Y. Fan, *Semicond. Semimetals*, 1967, **3**, 405–419.

34 H. Peelaers, E. Kioupakis and C. G. Van De Walle, *Appl. Phys. Lett.*, 2012, **100**, 2010–2013.

35 Y. Liu, J. M. Szeifert, J. M. Feckl, J. Rathousky, O. Hayden, D. Fattakhova-Rohlfing and T. BeinAcs, *ACS Nano*, 2010, **4**, 5373–5381.

36 G. E. Jellison, L. A. Boatner, J. D. Budai, B. S. Jeong and D. P. Norton, *J. Appl. Phys.*, 2003, **93**, 9537–9541.

37 Y. Furubayashi, T. Hitosugi, Y. Yamamoto, K. Inaba, G. Kinoda, Y. Hirose, T. Shimada and T. Hasegawaet, *Appl. Phys. Lett.*, 2005, **86**, 252101.

38 Y. Hirose, N. Yamada, S. Nakao, T. Hitosugi, T. Shimada and T. Hasegawa, *Phys. Rev. B: Condens. Matter Mater. Phys.*, 2009, **79**, 165108.

39 J. Zhuang, W. Dai, Q. Tian, Z. Li, L. Xie, J. Wang, P. Liu, X. Shi and D. Wang, *Langmuir*, 2010, **26**, 9686–9694.

40 Y. K. Lee, J. Park and J. Y. Park, *J. Phys. Chem. C*, 2012, **116**, 18591–18596.

41 B. Gholamkhass, K. Koike, N. Negishi, H. Hori, T. Sano and K. Takeuchi, *Inorg. Chem.*, 2003, **42**, 2919–2932.

42 C. Chen, W. Ma and J. Zhao, *Chem. Soc. Rev.*, 2010, **39**, 4206–4219.

43 J. Y. Huang, S. H. Li, M. Z. Ge, L. N. Wang, T. L. Xing, G. Q. Chen, X. F. Liu, S. S. Al-Deyab, K. Q. Zhang, T. Chen and Y. K. Lai, *J. Mater. Chem. A*, 2015, **3**, 2825–2832.

44 K. Chen, S. Zhou and L. Wu, *Chem. Commun.*, 2014, **50**, 11891–11894.

45 R. Blossey, *Nat. Mater.*, 2003, **2**, 301–306.

46 M. J. Powell, R. Quesada-Cabrera, A. Taylor, D. Teixeira, I. Papakonstantinou, R. G. Palgrave, G. Sankar and I. P. Parkin, *Chem. Mater.*, 2016, **28**, 1369–1376.

47 Z. Zhao, H. Tan, H. Zhao, D. Li, M. Zheng, P. Du, G. Zhang, D. Qu, Z. Sun and H. Fan, *Chem. Commun.*, 2013, **49**, 8958–8960.

48 R. Rahal, T. Pigot, D. Foix and S. Lacombe, *Appl. Catal., B*, 2011, **104**, 361–372.

This journal is © The Royal Society of Chemistry 2018